The Astrophysical Journal Letters, 983:L7 (15pp), 2025 April 10 https://doi.org/10.3847/2041-8213/adc30d

On the Million-degree Signature of Spicules

Souvik Bose[1,2,3,4], Jayant Joshi[5], Paola Testa[6], and Bart De Pontieu[1,3,4]
[1] Lockheed Martin Solar & Astrophysics Laboratory, Palo Alto, CA 94304, USA; bose@lmsal.com
[2] SETI Institute, 339 Bernardo Ave, Mountain View, CA 94043, USA
[3] Institute of Theoretical Astrophysics, University of Oslo, PO Box 1029, Blindern 0315, Oslo, Norway
[4] Rosseland Centre for Solar Physics, University of Oslo, PO Box 1029, Blindern 0315, Oslo, Norway
[5] Indian Institute of Astrophysics, II Block, Koramangala, Bengaluru 560034, India
[6] Harvard-Smithsonian Center for Astrophysics, 60 Garden St, Cambridge, MA 02193, USA
Received 2024 December 30; revised 2025 March 6; accepted 2025 March 11; published 2025 April 4

Abstract

Spicules have often been proposed as substantial contributors toward the mass and energy balance of the solar corona. While their transition region (TR) counterpart has unequivocally been established over the past decade, the observations concerning the coronal contribution of spicules have often been contested. This is mainly attributed to the lack of adequate coordinated observations, their small spatial scales, highly dynamic nature, and complex multithermal evolution, which are often observed at the limit of our current observational facilities. Therefore, it remains unclear how much heating occurs in association with spicules to coronal temperatures. In this study, we use coordinated high-resolution observations of the solar chromosphere, TR, and corona of a quiet-Sun region and a coronal hole with the Interface Region Imaging Spectrograph (IRIS) and the Atmospheric Imaging Assembly (AIA) to investigate the (lower) coronal (∼1 MK) emission associated with spicules. We perform differential emission measure analysis on the AIA passbands using basis pursuit and a newly developed technique based on Tikhonov regularization to probe the thermal structure of the spicular environment at coronal temperatures. We find that the emission measure (EM) maps at 1 MK reveal the presence of ubiquitous, small-scale jets with a clear spatiotemporal coherence with the spicules observed in the IRIS/TR passband. Detailed spacetime analysis of the chromospheric, TR, and EM maps show unambiguous evidence of rapidly outward-propagating spicules with strong emission (2–3 times higher than the background) at 1 MK. Our findings are consistent with previously reported MHD simulations that show heating to coronal temperatures associated with spicules.

Unified Astronomy Thesaurus concepts: Solar physics (1476); The Sun (1693); Solar atmosphere (1477); Solar corona (1483); Quiet solar corona (1992); Solar spicules (1525); Solar chromosphere (1479); Solar coronal heating (1989)

Materials only available in the online version of record: animations

1. Introduction

Spicules are thin, dynamic, thread-like features that appear ubiquitously on the surface of the Sun. They are one of the most abundantly observed features in the chromosphere, and their origin and role have long been a subject of debate (J. M. Beckers 1972; A. C. Sterling 2000; M. Carlsson et al. 2019; Hinode Review Team et al. 2019). Being ubiquitous, the mechanisms that drive spicules have held promise as contributing to coronal heating events (R. G. Athay & T. E. Holzer 1982; B. De Pontieu et al. 2011), and the chromospheric mass flux that these events propel to coronal heights is estimated to be 2 orders of magnitude higher than required to balance the mass loss due to solar wind (G. L. Withbroe 1983). It is estimated that at any given moment, the Sun's surface hosts at least a million spicules (J. M. Beckers 1972, and possibly significantly higher based on high-resolution observations) in active or quiet-Sun (QS) regions (P. G. Judge & M. Carlsson 2010) rapidly propagating outward.

Historically, spicules have mainly been observed in the chromospheric and transition region (TR) passband (J. M. Beckers 1972; K. P. Dere et al. 1989), but due to the lack of adequate high-resolution observations, a coronal counterpart was missing until high-resolution extreme ultraviolet (EUV) observations from space became available in the past decade. As a result, the possibility of energizing the solar corona through spicules was dismissed as unlikely in many of these early studies. The discovery of the short-lived and more dynamic (∼50–100 km s^{-1}) off-limb "type-II" spicules by B. De Pontieu et al. (2007) sparked renewed interest in their role of outer atmospheric heating since many of these spicules appeared to "fade" from the Hinode Ca II H passband, unlike their type-I counterpart. Such fading suggested a scenario where the opacity of Ca II H type-II spicules rapidly dropped during the spicule lifetime, possibly because of a combination of their dynamic evolution or even heating, to higher temperatures. Coordinated observations between Hinode and Atmospheric Imaging Assembly (AIA; J. R. Lemen et al. 2012) channels onboard NASA's Solar Dynamics Observatory (SDO; W. D. Pesnell et al. 2012), and later with the Interface Region Imaging Spectrograph (IRIS; B. De Pontieu et al. 2014) revealed that significant heating occurs in at least a subset of threads in type-II spicules along their whole length to TR temperatures (∼80,000 K; B. De Pontieu et al. 2011; T. M. D. Pereira et al. 2014). The on-disk counterparts of type-II spicules, termed rapid blue/redshifted excursions (RBEs and RREs; L. Rouppe van der Voort et al. 2009), were also associated with heating to at least TR (termed as network jets; H. Tian et al. 2014; L. Rouppe van der Voort et al. 2015) and possibly even coronal temperatures

(B. De Pontieu et al. 2011, 2017a; V. M. J. Henriques et al. 2016).

Despite substantial advancements in our understanding of the impact of spicules in the TR, their role in mass loading and heating the corona has remained a subject of significant debate both from an observational and a theoretical point of view. Several studies challenged their importance for the coronal mass and energy balance and argued that type-II spicules either play no role in coronal emission/heating (M. S. Madjarska et al. 2011) or their role is likely not a dominant one (D. Tripathi & J. A. Klimchuk 2013). This continued controversy is, in part, because the relatively poor resolution (compared to the size of the spicules) of existing coronal instruments has rendered it challenging to assess their impact on the coronal energy balance. Moreover, the presence of cooler (TR$<$0.5 MK) ions in the optically thin lines in the AIA passbands (B. O'Dwyer et al. 2010; J. Martínez-Sykora et al. 2011; G. Del Zanna & H. E. Mason 2018) renders an additional challenge because the observed emission could well be attributed to these "cooler" ions instead of $\geqslant$1 MK coronal emission. Furthermore, simplifying numerical assumptions (J. A. Klimchuk 2012; S. Sow Mondal et al. 2022) on the nature of the spicular plasma and the single-field-line approach of modeling spicules underestimates the complexity of the spicular environment, as evidenced by the complex processes involved in the coronal heating associated with spicules in multidimensional radiative MHD simulations (J. Martínez-Sykora et al. 2017).

The focus of this Letter is not on the contribution of spicules toward coronal heating, but rather we take a step back and attempt to investigate their $\sim$1 MK signature unambiguously, by targeting a QS and a coronal hole (CH) region, using coordinated IRIS and SDO/AIA observations. By narrowing our target to the above regions, we are most likely studying the $\sim$1 MK signature associated with type-II spicules since they are the more abundantly found in QS and CHs (T. M. D. Pereira et al. 2012). Therefore, unless otherwise mentioned, we refer to type-II spicules generally as spicules in this Letter. We exploit the high-resolution observations from IRIS to track the TR counterpart of (chromospheric) spicules and investigate their impact on the associated coronal structures, which can be observed in the form of propagating coronal disturbances (PCDs; B. De Pontieu & S. W. McIntosh 2010; T. Samanta et al. 2015; P. Bryans et al. 2016; S. Bose et al. 2023). Differential emission measure (DEM) analysis using two independent approaches is performed to study the thermal structure of the spicular plasma/PCDs within a temperature range centered around $\sim$1 MK.

2. Observations and Data Analysis

We use two coordinated IRIS–SDO/AIA observations, from 2014 September 24, targeting QS (henceforth data set 1) and CH (henceforth data set 2) regions. IRIS ran in a large sparse 16-step raster mode (`OBS id: 3823009186`) targeting a QS region (Figure 1(a)) centered around solar $(X,Y) = (211'', -238'')$ with $\mu = 0.94$ in data set 1 (μ being the cosine of the heliocentric angle). The duration of the data set was 2 hr and 6 minutes, starting at 18:09 UTC. Though IRIS provides spectra and simultaneous slit-jaw images (SJIs) in several spectral windows (see B. De Pontieu et al. 2014, for details), we concentrated on the chromospheric Mg II 2796 Å and the TR dominated Si IV 1400 Å SJIs in this study that had a field-of-view (FOV) spanning $120'' \times 120''$, a cadence of 38 s and a pixel scale of 0.″16, along with the rasters that had a cadence of 150 s (with a step cadence of 9.5 s, a step size of $1''$ and an exposure time of 8 s per slit position). The FOV covered by the rasters was $15'' \times 120''$ in the direction perpendicular and parallel to the slit direction as indicated in Figure 1(a). Data set 2 was recorded in a very large dense four-step raster mode (`OBS id: 3820257466`) targeting a CH region (Figure 2(a)) around solar $(X,Y) = (78'', -167'')$ with a roll angle of 90° in the counterclockwise direction. The value of μ was 0.98. The observed duration was $\approx$3 hr starting at 07:49 UTC. The Mg II 2796 Å and Si IV 1400 Å SJIs were recorded at a cadence of 11 s and with a FOV of $167'' \times 174''$. The rasters were acquired at a cadence of 21 s (with a step cadence of 5.4 s and 4 s exposure), with a step size of 0.″35 in the direction perpendicular to the slit covering a FOV of $1'' \times 174''$.

For each of the two IRIS data sets, we downloaded the co-temporal SDO/AIA observations to investigate the EUV response associated with spicules. These data sets were prepped, coaligned, and normalized using the standard `aiapy` (W. T. Barnes et al. 2020) routines. Additionally, the AIA images corresponding to data set 2 were rolled by 90° to have the same orientation as IRIS. The AIA data were further cropped, expanded (to IRIS SJI pixel scale), and spatially and temporally aligned to the respective IRIS SJIs by cross-correlating the (AIA) 1600 Å and (IRIS) Mg II 2796 Å channels. Panel (b) of Figures 1 and 2 show the coaligned AIA 171 Å images. We used the AIA data at the original pixel scale of 0.″6 for the DEM analysis. We defined 31 temperature bins from log T[K] = 5.5 to log T[K] = 7 in steps of 0.05 in log space for the Tikhonov regularization method by J. Plowman & A. Caspi (2020), and 21 temperature bins between log T[K] = 5.7 and log T[K] = 7.7 in steps of 0.1 (also in log space) for the sparse-matrix-based method by M. C. M. Cheung et al. (2015). The resulting EM maps, obtained from the two codes, were later coaligned to IRIS SJIs using the same parameters (shifts, crop, interpolation, etc.) as the AIA images. They are shown in panels (c) and (d) of Figures 1 and 2. The coaligned cubes were extensively visualized and analyzed with CRISPEX (G. Vissers & L. Rouppe van der Voort 2012), which is an IDL widget-based tool to visualize multidimensional data.

The propagation of spicules across the chromospheric, TR, and coronal channels was visualized by performing a spacetime analysis along multiple artificial slits in both SJIs and raster maps, as shown in Figures 1, 2, and 3. The slits were chosen after visually inspecting the animation of the coaligned data sets around the network regions where spicules are most abundant. Each slit is 10 IRIS pixels (1.″6) wide and has variable lengths ranging from $7''$ to $20''$. For the spacetime analysis on the raster, synthetic AIA and EM rasters were made that were spatially and temporally coaligned with the respective IRIS rasters. This was done to ensure consistency between the spectrograph observations, which need some time to "build" the FOV, while the AIA and EM images are instantaneous.

The IRIS Mg II k and Si IV 1402.77 Å spectra were fitted with double and single-Gaussian functions, respectively, to extract the corresponding intensities, Doppler shifts, and Mg II k_2 peak separation. We use the double-Gaussian fitting technique similar to the one employed by D. Schmit et al. (2015). Spicules on the solar disk are known to appear in absorption in the chromospheric Mg II spectra and have large line-of-sight (LOS) velocity gradients along with enhanced opacities and mass flows (S. Bose et al. 2019), which causes an

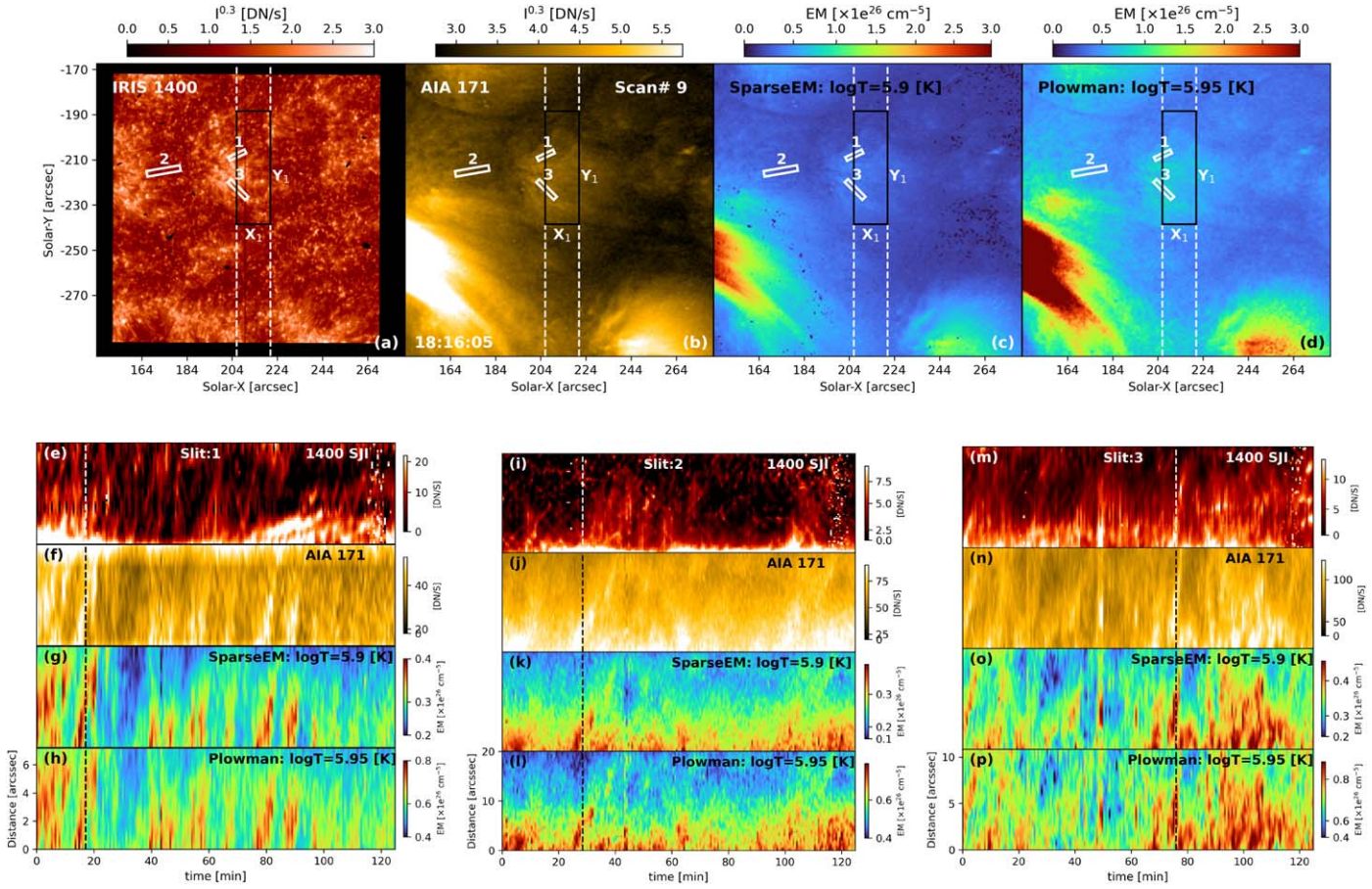

Figure 1. Overview of the coordinated IRIS–SDO/AIA QS data set 1 and the derived spacetime maps. Top row, panel (a): IRIS Si IV 1400 Å SJ image; panel (b): corresponding SDO/AIA 171 Å image; panel (c): EM map at log T[K] = 5.9 computed from the sparse-matrix method (M. C. M. Cheung et al. 2015); panel (d): EM map at log T[K] = 5.95 obtained from the Tikhonov regularization method (J. Plowman & A. Caspi 2020). The white dashed vertical lines in the above panels indicate the FOV covered by the IRIS rasters, and the rectangular region drawn in black indicates the region that is further analyzed in Figure 3. Panel (e): Si IV 1400 SJI spacetime map showing the propagation of the spicular plasma and their associated emission in the form of linear ridge-like structures derived using artificial slit "1"; panel (f): corresponding SDO/AIA 171 Å spacetime map; panels (g) and (h): spacetime maps corresponding to EM derived using the methods described in M. C. M. Cheung et al. (2015) and J. Plowman & A. Caspi (2020), respectively. Panels ((i)–(l)) and ((m)–(p)) are the same as panels ((e)–(h)) but for artificial slits "2" and "3." The white/black dashed vertical lines panels (e)–(p) correspond to the time step at which these maps are shown. An animation of this figure is available in the online journal, which shows the evolution of multiple network jets in the data set over 2 hr and 6 minutes in particular along the three artificial slits.
(An animation of this figure is available in the online article.)

enhancement in the k_2 peak separation (T. M. D. Pereira et al. 2013; P. Bryans et al. 2016). This makes visualizing spicules in k_2 peak separation maps easier than the intensity images. In the TR, spicules appear in emission in the form of network jets (H. Tian et al. 2014) with enhanced peak emission and nonthermal line broadening (L. Rouppe van der Voort et al. 2015). In this Letter, we focus on the Si IV peak and the Mg II k_3 intensity and Doppler shift, along with the k_2 peak separation.

3. Results

The animation associated with Si IV 1400 and AIA 171 channels in the top rows of Figures 1 and 2 show that the network regions at the footpoints of coronal loops are replete with spicule-like features. This scenario is consistent with several studies conducted in the past, such as P. Bryans et al. (2016), B. De Pontieu et al. (2017a), and S. Bose et al. (2023), where the coronal loops show significant complexities and are traditionally associated with PCDs. The spicule-like features, also termed as network jets in the TR (H. Tian et al. 2014; L. Rouppe van der Voort et al. 2015), can have apparent speeds in the range 40–200 km s^{-1} (N. Narang et al. 2016) and rapidly propagate outward. This is often followed by a downflowing (returning) phase (G. L. Withbroe 1983; S. Bose et al. 2021a, 2021b), where the spicules are seen to retract after reaching their maximum extent.

The reconstructed EM maps at ∼log T[K] = 5.9 (panels (c) and (d) of Figures 1 and 2) and their animation show features akin to AIA 171 observations. This is not surprising since the temperature bins of the EM maps shown in the figures are close to the peak temperature response (log T(K) ≈ 5.8; P. Boerner et al. 2012) of the 171 channel. However, unlike the AIA observations, which are often contaminated with ions formed at cooler (TR) temperatures (B. O'Dwyer et al. 2010; J. Martínez-Sykora et al. 2011; G. Del Zanna & H. E. Mason 2018), these maps show the amount of emission over the whole FOV (integrated along the LOS) within a narrow temperature bin centered at ∼log T[K] = 5.9 and are therefore better constrained than individual images. However, despite their widespread usage, EM inversions are not fully reliable at temperatures below log T[K] ≈ 5.6 (refer to the discussions in M. C. M. Cheung et al. 2015) due to the potential, but

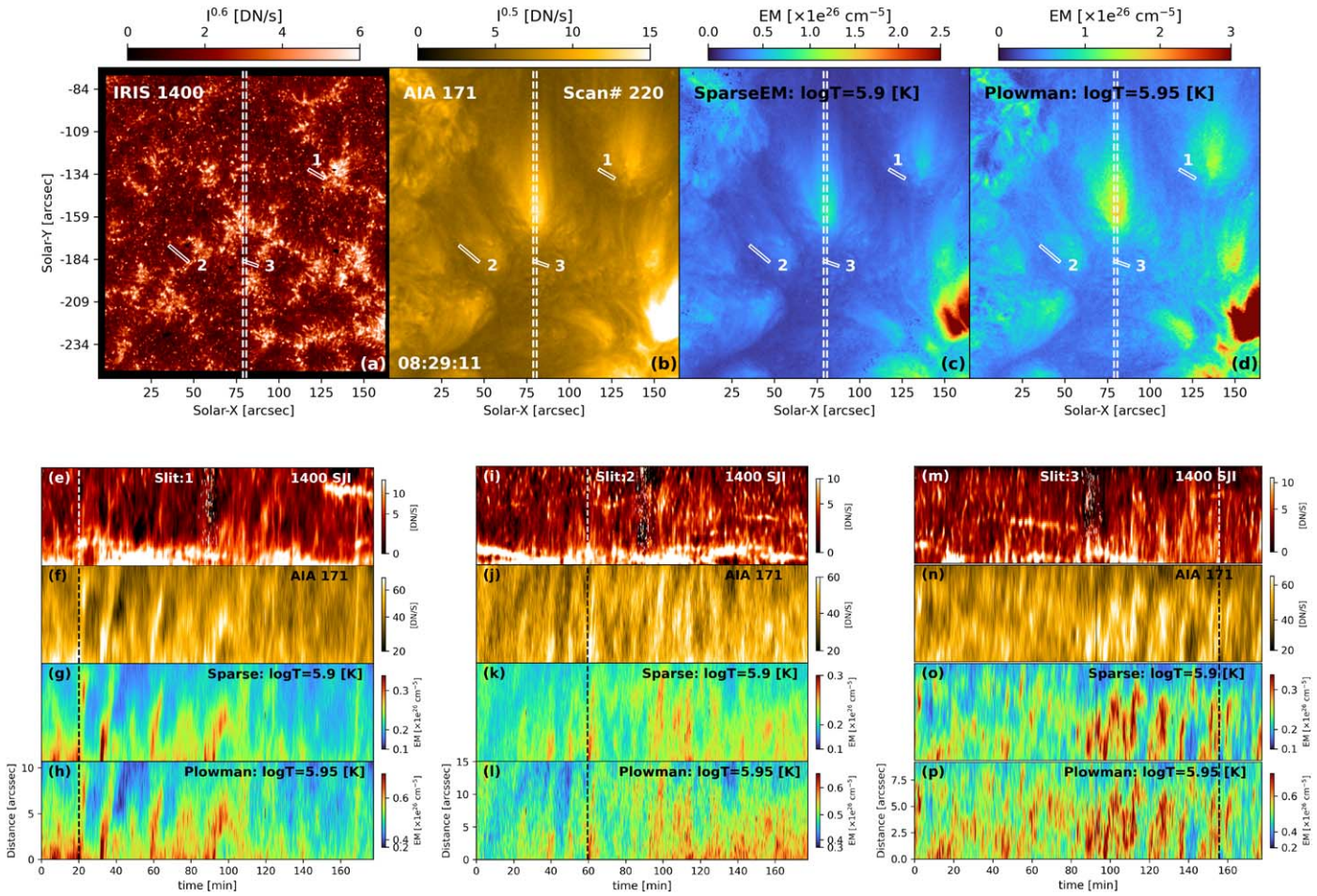

Figure 2. Overview of the coordinated IRIS–SDO/AIA coronal hole data set 2 and the derived spacetime maps. The format of this figure is the same as Figure 1 above. The FOV bounded by the IRIS raster is further analyzed in Figure 4. An animation of this figure is available in the online journal, showing the solar evolution and the dynamics of the network jets for 3 hr in the data set in the same format as Figure 1.

(An animation of this figure is available in the online article.)

ambiguous, low TR contributions to the AIA channels. Using two independent techniques, based on isothermal approximation (e.g., J. W. Cirtain et al. 2007) and filter-ratio diagnostics (e.g., N. Narukage et al. 2011; P. Testa & F. Reale 2020), we find that the minimum temperature associated with the emission of the spicular plasma at $\sim\log T[\mathrm{K}] = 5.9$ bin cannot be lower than $\log T[\mathrm{K}] = 5.7$ ($\approx$500 kK). We have discussed this in detail in Appendix A.

Spacetime maps generated from the artificial slits marked as 1, 2, and 3 are shown in panels (e)–(p) of Figures 1 and 2. Slits 1 and 3 in Figure 1 lie in the plume region as seen in the 171 Å channel (panel (b)) whereas slit 2 along with all the remaining slits in the top row of Figure 2 lie outside of plumes. They, however, lie in close vicinity of the network regions. These spacetime maps show abundant bright ridges with predominantly linear shapes, which are consistently visible across all the channels, including the Si IV SJI. The linear ridges indicate rapid, outward propagation along the slits. This outward propagation could either be caused by slow-mode magnetoacoustic waves in the low plasma-β TR and coronal environment (e.g., S. Krishna Prasad et al. 2012) or could be attributed to mass flows as suggested by B. De Pontieu & S. W. McIntosh (2010). It is difficult to distinguish between the two possibilities using only imaging data, and high-resolution spectroscopic observations are needed to interpret the picture fully. We refer to Section 4 for a brief discussion. In addition to the linear trajectories, some instances of parabolic paths traced by the spicules can also be seen in the spacetime maps, e.g., in Figures 2(f)–(h) between 75 and 85 minutes, and immediately afterward between 90 and 105 minutes, indicating the rising and falling phase of spicules. Although more commonly attributed to type-Is, parabolic trajectories lasting between 10 and 15 minutes are also widely observed in type-II spicules when multiwavelength observations covering a wide range of temperatures (chromospheric to TR/lower coronal) are considered (see, e.g., T. M. D. Pereira et al. 2014; T. Samanta et al. 2019). The emission (particularly the EM) associated with spicules is found to be substantially enhanced (roughly by a factor of 2 on average) compared with the time intervals where little-to-no spicular activity is observed (e.g., between 20 and 40 minutes in Figure 1(e)–(h)), but we notice a gradual drop in their emission as they propagate away from their source. This is also seen in the spacetime maps derived from the (synthetic) raster maps (Figures 3 and 4, described below).

The animations associated with the rasters in the left column in Figure 3 not only show spicules propagating in the chromospheric Mg II k_3 and TR Si IV channels (panels (a) and (b)), but also their corresponding propagation in the 171 Å and the two EM maps at $\sim\log T[\mathrm{K}] = 5.9$ (panels (c)–(e)). For the sake of brevity, we only show a portion of the raster FOV

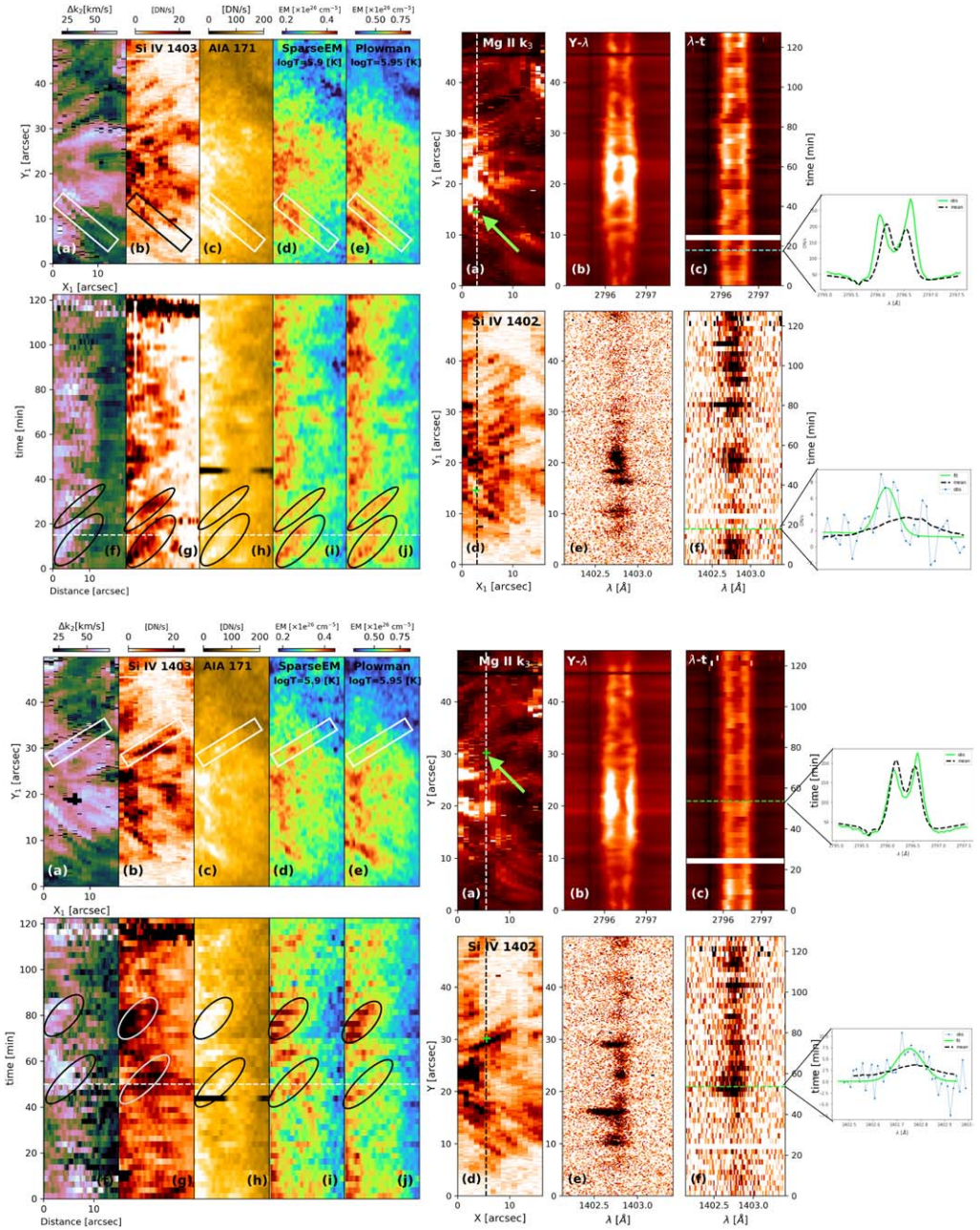

Figure 3. Propagation of spicules in the chromosphere, TR, and lower corona (∼1 MK) as observed from a portion of the raster map (black rectangular region in Figure 1) and their corresponding Mg II k and Si IV spectra. Left column, panel (a): Mg II k_2 peak separation map; panel (b): peak intensity map derived from Si IV 1402.77 Å spectra; panel (c): synthetic SDO/AIA 171 rasters; panel (d): synthetic sparse EM rasters; panel (e): synthetic Tikhonov EM rasters, corresponding to the IRIS rasters. The rectangular boxes in (a)–(e) show the FOV from which the corresponding spacetime maps shown in panels (f)–(j) are derived. The ovals shown in the spacetime maps exemplify the chromospheric-TR-lower coronal connection associated with some spicules. Right column, panel (a): intensity in Mg II k_3 derived from bi-Gaussian fit; panel (d): peak intensity of Si IV 1402.77 Å spectra derived from single-Gaussian fit; panel (b): spectral-space (λy) diagram of Mg II; panel (e): λy diagram of Si IV, obtained along with vertical slice denoted by dashed lines in panels (a) and (d); panel (c): corresponding Mg II spectral-time (λt) diagram; panel (f): corresponding Si IV λt diagram of the location indicated by the green arrow in panels (a). The inset figures show the Mg II and Si IV spectra at a couple of instances in time. An animation of this figure is also available in the online journal, which shows the propagation of spicules/network jets across multiple wavelength channels along with the evolution of their spectra covering roughly 120 minutes of solar time.

(An animation of this figure is available in the online article.)

from data set 1 indicated by the black bounded region in Figure 1, which has the highest spicule density. To further visualize their propagation we choose two additional (artificial) slits of the same size in the raster maps and show the corresponding spacetime plots in panels (f)–(j). Like the SJI spacetime maps, we find linear ridges of enhanced TR and coronal emission associated with spicules that can now also be visualized in the Mg II k_2 peak separation spacetime maps (panel (f)). Due to the relatively low cadence (150 s) of the rasters compared to the SJIs, it is difficult to capture the complete evolution of all spicules, many of which last well below 100 s in the chromosphere (T. M. D. Pereira et al. 2012; S. Bose et al. 2021a). Nonetheless, we see a few examples in both the spacetime maps marked with ellipses in the left

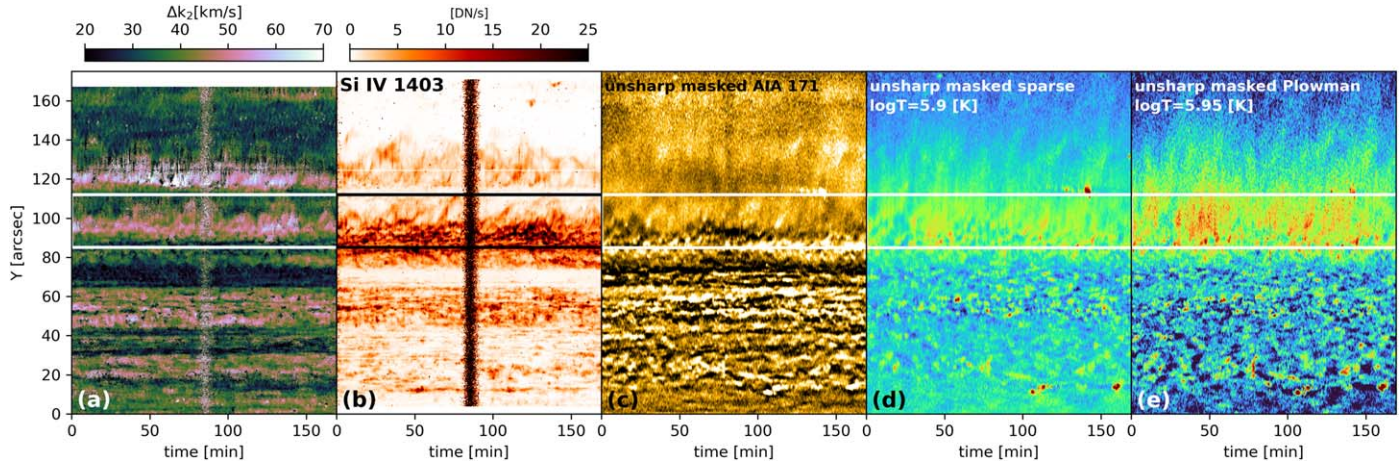

Figure 4. Propagation of spicules in the chromosphere, TR, and lower corona (~1 MK) as observed from the raster in Figure 2. Panel (a): Mg II k_2 peak separation. Panel (b): Si IV 1402.77 Å peak intensity. Panel (c): unsharp masked SDO/AIA 171 Å intensity; panel (d): unsharped masked EM computed using the method of sparsity; and panel (e): unsharped masked EM computed using Tikhonov regularization. The region bounded by two horizontal solid lines is analyzed further in Figure 12 in Appendix B.

column of Figure 3. For instance, the enhanced emission ridge between $t = 7$–19 minutes and $t = 25$–30 minutes in the top row, and between $t = 45$–50 minutes and around $t = 79$ minutes in the bottom row shows the propagation in the coronal channel associated with chromospheric and TR counterpart of spicules quite distinctly. Additionally, we find repetitive coronal emission patches (non-ridge-like) between 0″ and 10″ in the spacetime maps throughout the entire 120 minutes of observation. These patches are also likely associated with spicules as evidenced by their enhanced Mg II k_2 peak separation, but their evolution is not fully captured owing to the low temporal resolution of the rasters. Upper chromospheric velocities derived from the Doppler shift of Mg II k_3 and their spacetime maps (Figure 11 in Appendix A and their animation) show velocities ranging between 20 and 30 km s^{-1} (through the shifts in the Mg II k_3 core with respect to the rest-frame k_3 wavelength of 2796.352 Å in vacuum[7]) at the footpoints of the coronal structure. Being a complex, optically thick spectral line, determining the actual Doppler shifts in Mg II associated with spicules is a nontrivial task since opacity effects strongly impact these profiles (S. Bose et al. 2019). Nonetheless, the values of Doppler shifts are consistent with recent observations of RBEs and RREs in Mg II, for example, by S. Bose et al. (2019) and V. L. Herde et al. (2023).

The right column of Figure 3 shows two spectral-time (λt, panels (c), and (f)) diagrams and co-temporal spectrograms (λy, panels (b), and (e)) in Mg II and Si IV spectra at the locations marked along the two slits shown in panels (a) and (d). The slits are chosen based on the location of the spacetime analysis discussed in the previous paragraph. Panels (a), (b), (d), and (e) in the top and bottom right corners of Figure 3 are shown at instants indicated in the corresponding λt diagrams. The Mg II k_3 intensities and λy spectrograms in Figure 3 show the occurrence of many spicules and their associated spectral excursions. The spicule spectra in Mg II can readily be identified by the Doppler shift (excursion) of the central absorption k_3 feature and the corresponding suppression (enhancement) of the respective k_2 peaks, as shown in the inset figures. This is consistent with the analysis presented in L. Rouppe van der Voort et al. (2015) and S. Bose et al. (2019).

[7] Source: https://physics.nist.gov/PhysRefData/ASD/lines_form.html.

The λt diagrams in Figure 3 panel (c) show the repetitive occurrence of the short-lived asymmetries at the location indicated by a plus sign in panel (a). The Si IV 1402.77 Å spectra are noisier at this exposure (refer to the inset figures); however, comparing panels (d)–(f) with (a)–(c) and their animation, we find very similar spatiotemporal behavior with blue and redshifts of the line center in tandem with the Mg II k counterparts. Single-Gaussian fits to the Si IV 1402.77 Å spectra (see inset panels) reveal Doppler shifts in the range 12–20 km s^{-1}.

Analysis of the raster maps derived from data set 2, shown in Figure 4, reveals a consistent scenario where the chromosphere is replete with spicular mass flows that originate in the close vicinity of the network or the footpoint of the coronal plume (between $Y = 85''$ and 117″, panel (a)). These regions are also naturally accompanied by strong Si IV peak emission shown in panel (b) owing to the presence of network jets. To accentuate the propagating features, we show an unsharped masked version of the 171 Å and the EM maps (panels (c)–(e)). These panels reveal the ubiquitous signature of linear ridges with a high EM throughout the entire 165 minutes. Figure 12 in Appendix B zooms into the above region and shows the presence of strong Doppler shifts in the Mg II k_3 associated with areas of enhanced k_2 peak separation.

Panels (a) and (b) in Figure 4 show a separate region of spicular activity around $Y = 120''$, which upon examining the Si IV SJI in Figure 2(a), shows the presence of an enhanced spicular activity due to the small patch of network elements. This difference is not obvious in the corona (refer to Figure 4(c)–(e)) due to long, overlying plume structures originating around $Y = 85''$ seen in the AIA 171 image in Figure 2(b). However, enhanced emission ridges can be seen in Figures 4(c)–(d) between $Y = 120''$ and 140″, which are likely their lower coronal counterparts. Interestingly, the region immediately below $Y = 80''$ is devoid of any spicular ridges in the raster maps, which is further supported by the reduced Mg II k_2 peak separation and Si IV peak emission. The Si IV SJI confirms the scenario where spicular features are also absent. The traces of enhanced Mg II k_2 peak separation and Si IV emission observed between $Y = 20''$ and 60″ in Figure 4 are only due to a (small) portion of the spicules overlapping the IRIS slit and originating around $X = 90''$ seen in Figure 2 panel (a). Unlike the spicules

discussed above, they are not oriented along the slit and hence appear as patches instead of elongated ridges in the spacetime raster map in Figure 4.

4. Discussion and Conclusion

Ever since the discovery of the more energetic type-II spicules in 2007 (B. De Pontieu et al. 2007) speculations about their contribution toward heating and mass loading of the solar corona have been a topic of significant interest and debate (see, e.g., B. De Pontieu et al. 2011; M. S. Madjarska et al. 2011; J. A. Klimchuk 2012; P. Bryans et al. 2016; B. De Pontieu et al. 2017a; T. Samanta et al. 2019; S. Bose et al. 2023). This Letter does not attempt to answer whether spicules play any role in heating the corona as a whole but it presents unique observational evidence that suggests the plasma associated with a subset of spicules can be heated to a million degrees. Based on a selection of targets (i.e., QS and CH) and the fact that heating to TR and lower coronal temperatures are involved (M. Carlsson et al. 2019), it is very likely that the spicules investigated in this Letter are of the type-II category. The basis of this investigation lies in computing DEM inversions of QS and CH data using two independent algorithms—one based on L^1 norm (M. C. M. Cheung et al. 2015) and the other on L^2 norm (J. Plowman & A. Caspi 2020). The two algorithms differ mainly in minimizing the objective function to obtain the DEMs and, therefore, serve as an independent way to detect the million-degree emission associated with spicular plasma. The major advantage of this approach is the ability to quantify the amount of emission in a specific temperature bin, which is impossible to infer directly from the AIA images owing to the contamination from cooler TR ions (J. Martínez-Sykora et al. 2011; G. Del Zanna & H. E. Mason 2018). To strengthen our claims, we investigate the impact of potential (cooler) TR contamination in the AIA emission associated with network jets using isothermal approximation and filter-ratio diagnostics (see Appendix A). Our analysis shows that network jets observed in the AIA passbands can have strong emissions above $\log T[\mathrm{K}] = 5.7$ or ≈500,000 K, up to at least 1 MK. The representative examples presented in Figures 7, 8, 9, and 10 show that even under simplistic assumptions, we can constrain the emission measure in the range $\log T[\mathrm{K}] = [5.5, 5.7]$. This further enhances confidence in the results obtained using standard DEM inversions around $\log T[\mathrm{K}] \approx 5.9$ presented in this Letter.

To the best of our knowledge, this is the first time DEM inversions have been applied to study the lower coronal response associated with type-II spicules/network jets in such detail. Recently, S. Mandal et al. (2023) applied the method of M. C. M. Cheung et al. (2015) to investigate the lower coronal response of dynamic fibrils (or type-I spicules) with coordinated IRIS, SDO, and Extreme Ultraviolet Imager's Fe IX 174 Å observations. Though their analysis suggests that some dynamic fibrils may be heated to >1 MK, further investigation of the TR contamination and temporal evolution is needed to draw firm conclusions on their exact temperature. Moreover, the dynamic fibrils appear as roundish bright blobs in the 174 Å channel (resembling the "grains" in IRIS Si IV passband; H. Skogsrud et al. 2016) that have a different morphology than the examples presented in this Letter.

Animation of the EM maps, Si IV SJIs, and AIA 171 Å images along with the spacetime analysis presented in this Letter clearly show a spatiotemporal coherence with spicules/network jets observed in the IRIS passband and a strong EM around $\log T[\mathrm{K}] = 5.95$ associated with the propagation of the plasma associated with spicules. It is to be noted that the EM obtained from the method of sparsity (L^1 norm) is on average lower than that obtained from L^2 norm for a given temperature bin due to the latter's tendency to prefer a flat DEM (in absence of other constraints) compared to minimizing the DEMs (in case of sparsity) as described in J. Plowman & A. Caspi (2020). Nonetheless, both codes provide consistent results where the EM associated with spicular plasma is nearly 2–3 times higher than the respective background emission, which is not observed in the case of dynamic fibrils (e.g., S. Mandal et al. 2023).

Our observations are consistent with a scenario where abundant spicular activity is found in the chromospheric and TR passbands rooted close to the footpoints of the coronal loops (S. Bose et al. 2023). Moreover, the relationship between spicules setting off PCDs that has been proposed in multiple studies (e.g., in T. Samanta et al. 2015; B. De Pontieu et al. 2017a; K.-S. Cho et al. 2023) is further enhanced. Numerical modeling predictions from J. Martínez-Sykora et al. (2017), B. De Pontieu et al. (2017a), and J. Martínez-Sykora et al. (2018) suggest that the observed PCDs are likely governed by a complex chain of events involving the generation of spicular flows and associated shock waves, along with heating of plasma through the dissipation of electrical currents and that PCDs are not necessarily caused by magnetoacoustic waves alone. Furthermore, the spacetime maps (particularly in Figures 1 and 2) show a gradual decrease in the enhancement of the EM associated with PCDs as the disturbances propagate higher up in the corona. This is likely due to the smearing of the density and the temperature of the spicular plasma owing to thermal conduction (J. Martínez-Sykora et al. 2018).

The animation associated with Figure 11 in Appendix B shows consistent LOS velocities on the order of 20–30 km s^{-1} in the upper chromosphere along with enhanced Mg II k_2 peak separation. The range of the derived Doppler shifts is consistent with the values observed in RBEs and RREs in other chromospheric lines such as Ca II 8542 Å and Hα (D. H. Sekse et al. 2013). The Doppler shifts measured from Si IV are comparable with L. Rouppe van der Voort et al. (2015) but we note that single-Gaussian fitting may not always catch the full complexity of these profiles. Recent studies (e.g., P. Kayshap et al. 2018; J. Gorman et al. 2022) suggest that sometimes an extra velocity component of ∼50–70 km s^{-1} may be found in the far wings of the Si IV spectral line. In addition, the impact of different viewing angles between the local magnetic field direction or flows and the LOS may be significant and difficult to determine from a single viewpoint observation. Interestingly, from Figure 5, we notice that the apparent velocities of the coronal signal projected into the plane of the sky are primarily between 15 and 45 km s^{-1} and that the Doppler shifts in k_3 of Mg II are similar. We note that the actual Doppler shifts of the chromospheric plasma may be higher than those derived from the k_3 core spectral feature since that is part of a complex profile in an optically thick line.

If mass flows indeed cause the plane-of-sky motions, they would be compatible with a scenario in which real flows of order 40 km s^{-1} are observed with a viewing angle of order 45° (between the magnetic field vector and the LOS), leading to Doppler shifts in the upper chromosphere of 20–30 km s^{-1} (as seen in Mg II k_3), and projected velocities in the plane of the sky in coronal images of 20–30 km s^{-1}. Alternatively, if the

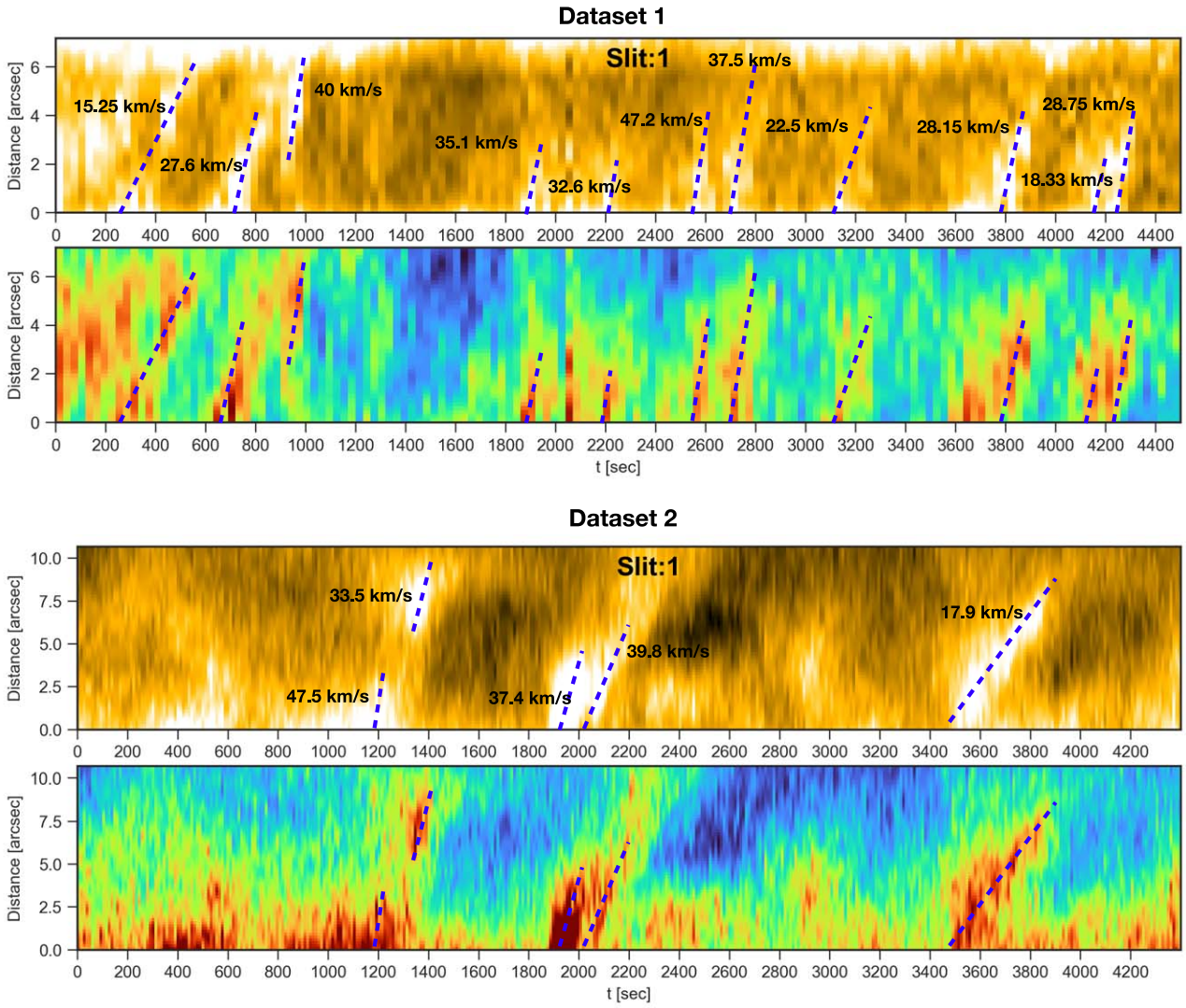

Figure 5. Coronal plane-of-sky velocities corresponding to the x–t maps of slit-1 from data sets 1 (top row) and 2 (bottom row) shown in Figures 1 and 2. The x-axis shows the time in seconds from the beginning of the observation. The dashed blue lines indicate the propagation for which the velocities are indicated. The two panels in each of the two rows correspond to SDO/AIA 171 Å and EM map derived using Tikhonov regularization.

apparent coronal motions are caused, by, e.g., a sound wave of thermal conduction front (e.g., B. De Pontieu et al. 2017b), the viewing angle would be 60° or higher since field-aligned speeds of waves or conduction fronts are expected to be of order 100 km s^{-1} or more.

The λt and λy slices of the Si IV spectra shown in the right column of Figure 3, along with its animation, show similar spatiotemporal behavior with blueshifted(redshifted) excursions in tandem with the Mg II k line. This behavior reaffirms the findings of L. Rouppe van der Voort et al. (2015) and suggests that the network jets are the TR counterparts of chromospheric RBEs and RREs.

The results presented in this Letter highlight the multithermal nature of type-II spicules (similar to B. De Pontieu et al. 2011; T. M. D. Pereira et al. 2014; S. Bose et al. 2021b; G. Chintzoglou et al. 2021, to name a few) along with their complex spatiotemporal evolution where a significant fraction of the plasma associated with spicules is heated to a million degrees with a lower temperature threshold of about 500,000 K. This conclusion is based on a comprehensive DEM analysis of two (QS and CH) data sets using two independent algorithms. This is the first time multiple DEM-based approaches have been applied to type-II spicules to study their emission in the lower corona in such detail. Our results are compatible with predictions from previously reported advanced numerical models (J. Martínez-Sykora et al. 2017, 2018, 2020) that show heating to TR and coronal temperatures associated with spicules. Moreover, the computed synthetic TR and coronal images, e.g., in J. Martínez-Sykora et al. (2018), show remarkable similarities to the brightenings seen in TR and coronal passband observed in the current study. The generation of the simulated type-II spicules in the above papers drive Alfvénic waves and electric currents that travel along the magnetic field. The dissipation of such waves and/or currents leads to heating of the associated plasma to TR and coronal temperatures, and the whole process leads to synthetic PCDs

similar to our observations. This Letter is therefore a step ahead of previous studies (owing to the DEM-based approaches and an independent determination of the contribution from cooler TR ions), and the results do not exclude the possibility that spicules do indeed play a role in energizing the lower solar corona, which remains a widely debated topic in the community. To fully resolve this issue will require coordinated, high-resolution observations covering multiple layers of the solar atmosphere (at a high cadence). This is not an easy task because the spatiotemporal properties of spicules are often at the limit of many current instrumentation capabilities. High-resolution coronal spectroscopic observations from the upcoming NASA's Multi-slit Solar Explorer (MUSE; B. De Pontieu et al. 2020, 2022) mission, Solar-C EUVST, in coordination with IRIS and ground-based data such as DKIST and SST would be the obvious next step in understanding if any heating along coronal loops is linked to spicular injection at its base. MUSE's comprehensive spectroscopic coverage, encompassing the entire length of coronal loops and their footpoints, would allow for reconstructing their complete thermodynamic history. This includes the preceding phase of spicule activity, the subsequent dissipation of currents or waves within the loops, and the final cooling stages. We look forward to such developments.

Acknowledgments

IRIS is a NASA small explorer mission developed and operated by LMSAL with mission operations executed at NASA Ames Research Center and major contributions to downlink communications funded by ESA and the Norwegian Space Centre. S.B. gratefully acknowledges support from NASA's SDO/AIA contract (NNG04EA00C), and S.B. and B. D.P. acknowledge support from the IRIS contract (NNG09FA40C) to LMSAL. J.J. acknowledges funding support from the SERB-CRG grant (CRG/2023/007464) provided by the Anusandhan National Research Foundation, India. PT is funded for this work by contract 8100002705 (IRIS) to the Smithsonian Astrophysical Observatory. We acknowledge fruitful discussions with Marc De Rosa while preparing the manuscript.

Software: SunPy (W. T. Barnes et al. 2020), SciPy (P. Virtanen et al. 2020), Matplotlib (J. D. Hunter 2007), Numpy (C. R. Harris et al. 2020), SSWIDL.

Appendix A
Determining the Lower Temperature Cutoff in Network Jets

In this appendix, we discuss two approaches that we used to constrain and estimate the contribution of the lower transition region to the DEM analysis, given its potential contributions to the AIA passbands. The ambiguity in DEM results from AIA is caused by the known TR contamination of the AIA passbands. We used IRIS observations and applied two methods to help constrain this contribution: an isothermal approximation of the plasma as well as filter-ratio diagnostics. In both cases, we compute the EM from the two methods ($EM_{derived}$) and compute the predicted intensity (counts) associated with network jets as would be observed in IRIS Si IV SJI, assuming it is dominated by Si IV 1402.77 Å. In principle, we use

$$I_{pred} = EM_{derived} \times R, \quad \text{(A1)}$$

where $R = R_{Si\ IV}$ is the response function of the Si IV 1402.77 Å line computed using `isothermal.pro` routine, which is available in CHIANTI v10.1 (K. P. Dere et al. 2023) in SSWIDL. We assumed coronal abundances (Sun_coronal_2021_chianti.abund from M. Asplund et al. 2021), an electron number density of $10^{10}\,cm^{-3}$ that is typical in Si IV around log $T[K] = 4.9$ under nonflaring conditions (e.g., P. R. Young et al. 2018). To convert the synthetic Si IV spectra from physical [Photon $cm^{-2}\,s^{-1}\,sr^{-1}\,px^{-1}$] units to [DN $s^{-1}\,px^{-1}$], we use the effective areas and photon to DN conversion values of IRIS SJI in Si IV from `iris_get_response.pro`. The response functions (R) of the Si IV line and selected SDO/AIA channels are shown in Figure 6.

Isothermal Approximation. Assuming that the emitting plasma is isothermal, Equation (A1) can be used to obtain the total source EM by dividing the observed intensity by the response function at a given temperature. The following steps determine the lower temperature cutoff associated with spicular plasma emitted in log $T[K] = 5.9$. We:

1. Calculate the EM at $\log T[K] = 5.9$ (say $EM_{5.9}$) by dividing the observed intensity (in a network jet) by the respective AIA filter response functions ($R_{5.9}$) at this temperature.
2. Consider a hypothetical scenario where the emission observed above has been incorrectly assigned to EM at $\log T[K] = 5.9$ but is instead due to a contribution from a lower temperature (e.g., $\log T[K] = 4.9$). To satisfy this requirement, $EM_{4.9} = EM_{5.9} \times \frac{R_{5.9}}{R_{4.9}}$, where $R_{4.9}$ is AIA filter response at $\log T[K] = 4.9$.
3. Use Equation (A1) to compute predicted Si IV 1402.77 Å intensity at $\log T[K] = 4.9$ using the response function shown in Figure 6 and the derived $EM_{4.9}$ to compare the result with observed intensity in IRIS Si IV 1400 Å SJI.
4. If the predicted intensity (at $\log T[K] = 4.9$) is comparable to the observed value (with IRIS), it is likely that the observed intensity in the AIA channels is due to the emission from the cooler TR component observed by IRIS. Otherwise, if the predicted intensity is much larger than the observations, the cooler TR contamination in AIA is unlikely.

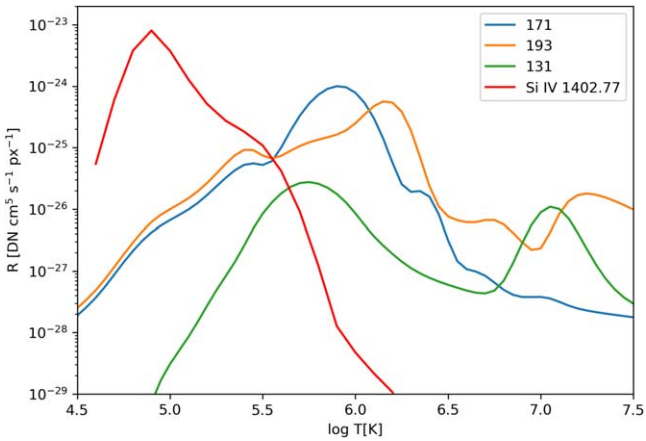

Figure 6. Response functions for Si IV and SDO/AIA 131, 171, and 193 Å EUV channels. The response functions for the (selected) AIA channels are calculated using the routines available in SSWIDL, and the Si IV line is calculated using the method described in the appendix.

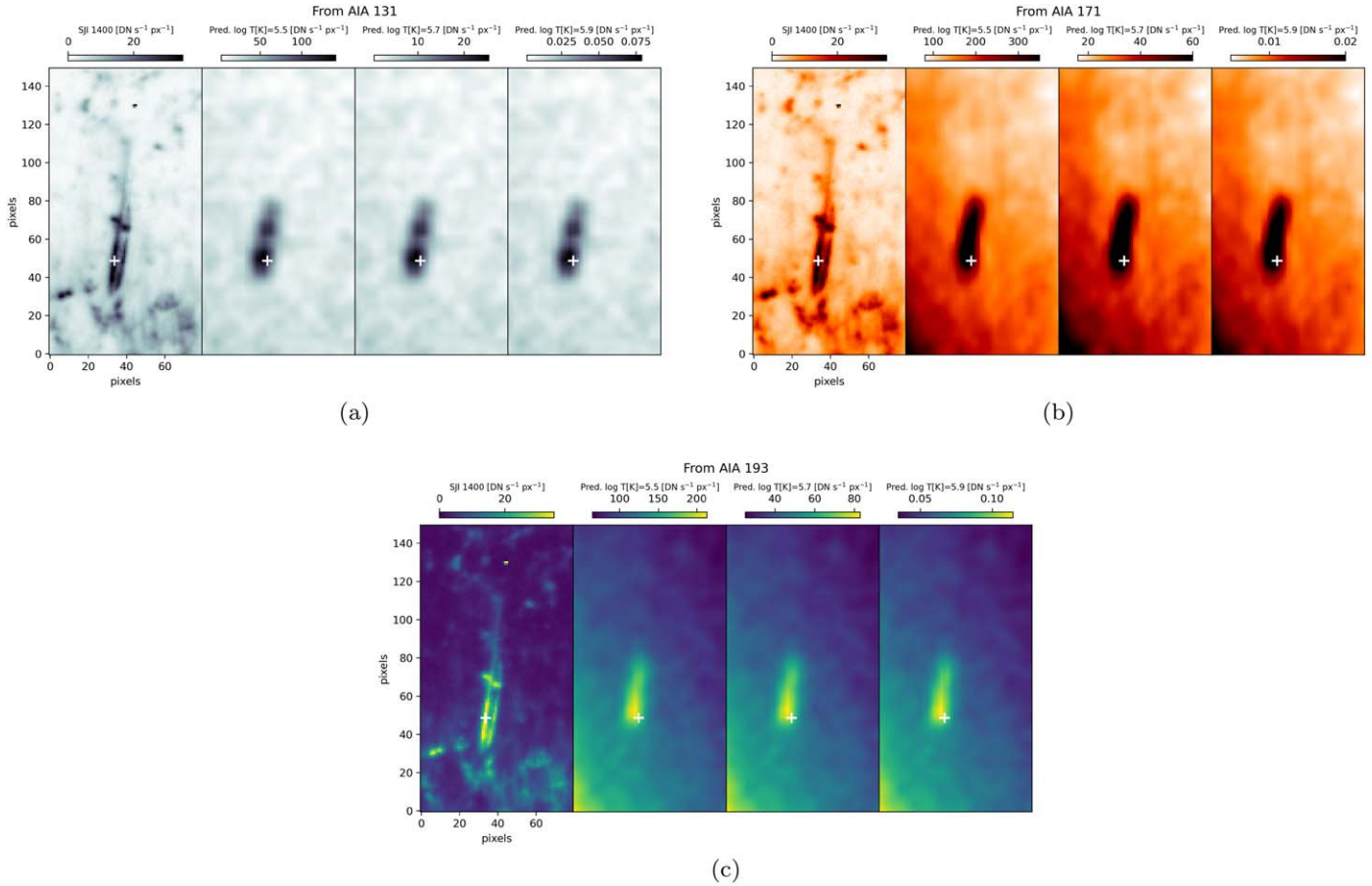

Figure 7. Representative example of a network jet observed in coordinated IRIS and SDO/AIA data set 1 to illustrate the (cooler) TR contamination in the AIA passbands. Predicted counts in different temperature bins obtained under isothermal approximation are shown for AIA 131 Å in panel (a), AIA 171 Å in panel (b), and AIA 193 Å in panel (c). The leftmost image in each of the panels shows the observed IRIS Si IV 1400 counts for comparison, and the "plus" marker serves as a guide for locating the same pixel across the different images. Note the different color bars in each of the images, which were intentionally chosen to optimize the visualization of the network jet. The size of each pixel is 0.″167 in the horizontal and vertical direction.

The above steps are repeated for a range of temperature values between $\log T[\mathrm{K}] = [4.9, 5.9]$ in intervals of 0.1 for the three AIA channels (131, 171, and 193) over the whole FOV. This analysis did not include AIA 211, 335, and 94 Å because of their relatively low sensitivity below $\log T[\mathrm{K}] = 5.7$. We show three illustrative examples of network jets in Figures 7, 8, and 9, where we follow the approach outlined above and show a comparison of the observed IRIS Si IV SJI and predicted intensities in three temperature bins, i.e., $\log T[\mathrm{K}] = 5.6$, 5.7, and 5.9. The examples clearly indicate that the predicted range of intensities at $\log T[\mathrm{K}] = 5.7$ best resembles the IRIS SJI 1400 Å observations, while at temperature bins lower and higher than $\log T[\mathrm{K}] = 5.7$, a clear mismatch with observations is seen. Moreover, the AIA signal does not extend over the same spatial range as the IRIS observations, suggesting that the predicted intensities are not a simple print-through of the IRIS passband. In other words, the emission in the AIA passbands cannot be only due to the cooler TR contaminants. Therefore, this analysis strongly suggests that the lower temperature cutoff (or the relatively cool TR contamination) in the network jets observed in the AIA channels cannot be below $\log T[\mathrm{K}] = 5.7$ or ≈500,000 K.

Filter-ratio diagnostic. The filter ratio (of the different AIA temperature response functions) is a popular diagnostic that has been extensively used (see, e.g., N. Narukage et al. 2011, for a detailed discussion) to provide a fast and an approximate way to determine the coronal temperatures using the observed intensity ratio in the corresponding filters. Here, we use the filter ratio in the AIA 171 and 131 passbands within $\log T[\mathrm{K}] = [5.5, 6]$ to determine the temperature. The choice of this range is based on the (approximate) linear dependence of the filter ratio with temperature, which allows for a unique determination of the temperature. Once the temperature is determined, the total EM can be determined by dividing the observed intensity in 171 (or 131) by the corresponding response (R) at that temperature. Finally, the total EM is folded with the R of Si IV 1402.77 Å using Equation (A1) to obtain the predicted intensities.

Figure 10 panel (a) shows the AIA 171 and 131 passbands' filter-ratio and temperature dependence. Between $\log T[\mathrm{K}] = [5.55, 6.0]$, the ratio is approximately linear and monotonically increasing, which allows us to uniquely determine the temperature of the three network jets shown in panels (b)–(d). The morphology of the network jets appears similar in the maps of predicted intensities and temperature. They allow us to conclude that the minimum temperature associated with the three network jets is around $\log T[\mathrm{K}] = 5.7$, which corresponds with the minimum temperature values derived from the isothermal approximation approach in the previous section. Interestingly, we also find a variation in the derived temperature along the length of the network jets 1 and 3, where temperatures around $\log T[\mathrm{K}] = 5.9$ are also seen.

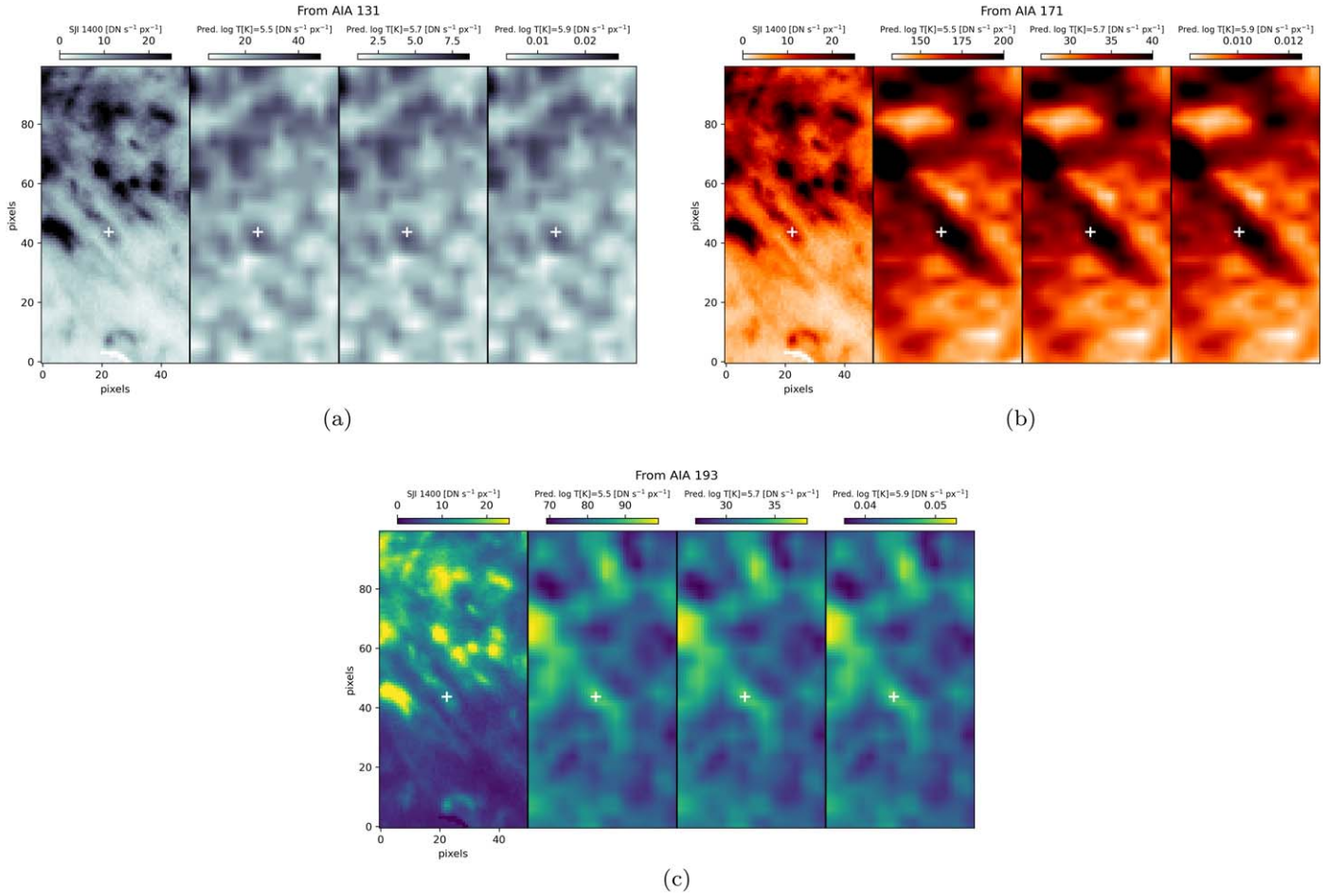

Figure 8. Same as Figure 7 but for a different network jet observed in data set 1.

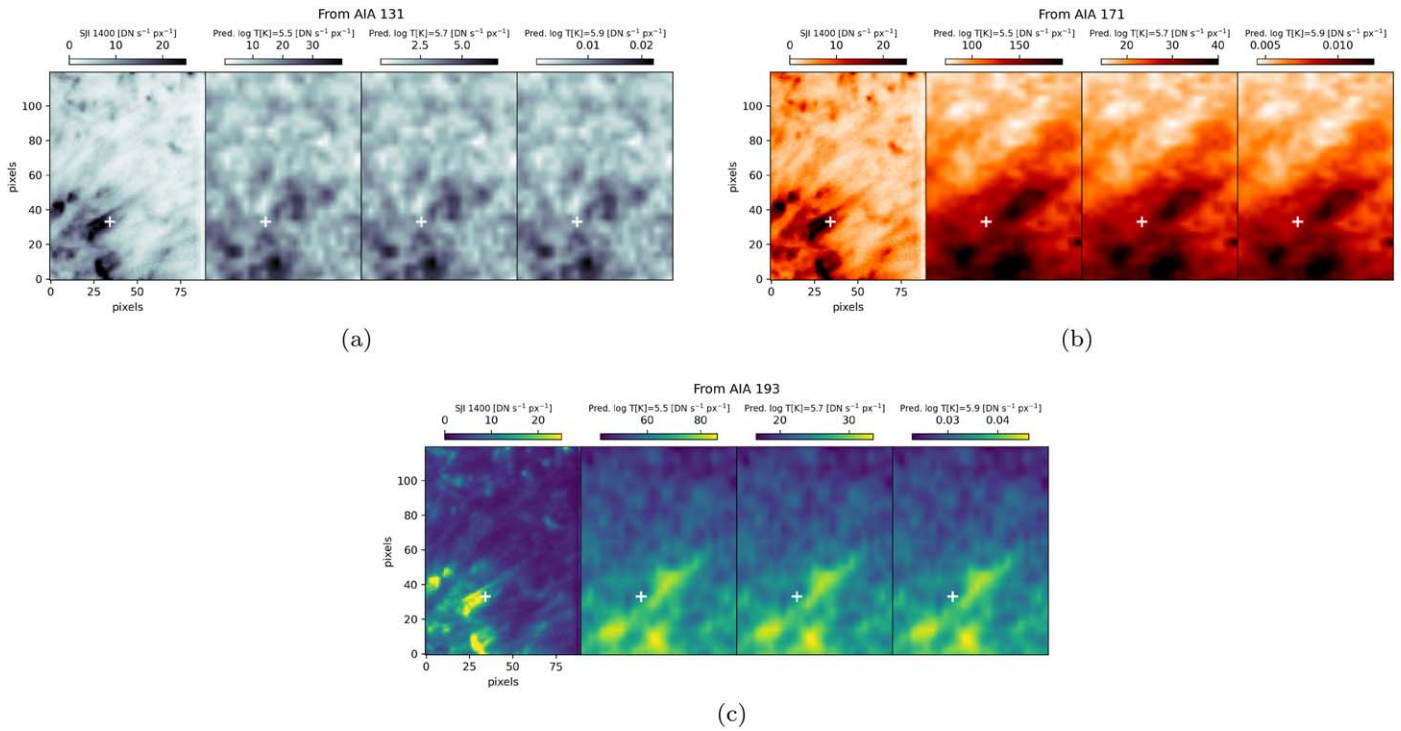

Figure 9. Same as Figure 7 but for a different network jet observed in data set 2.

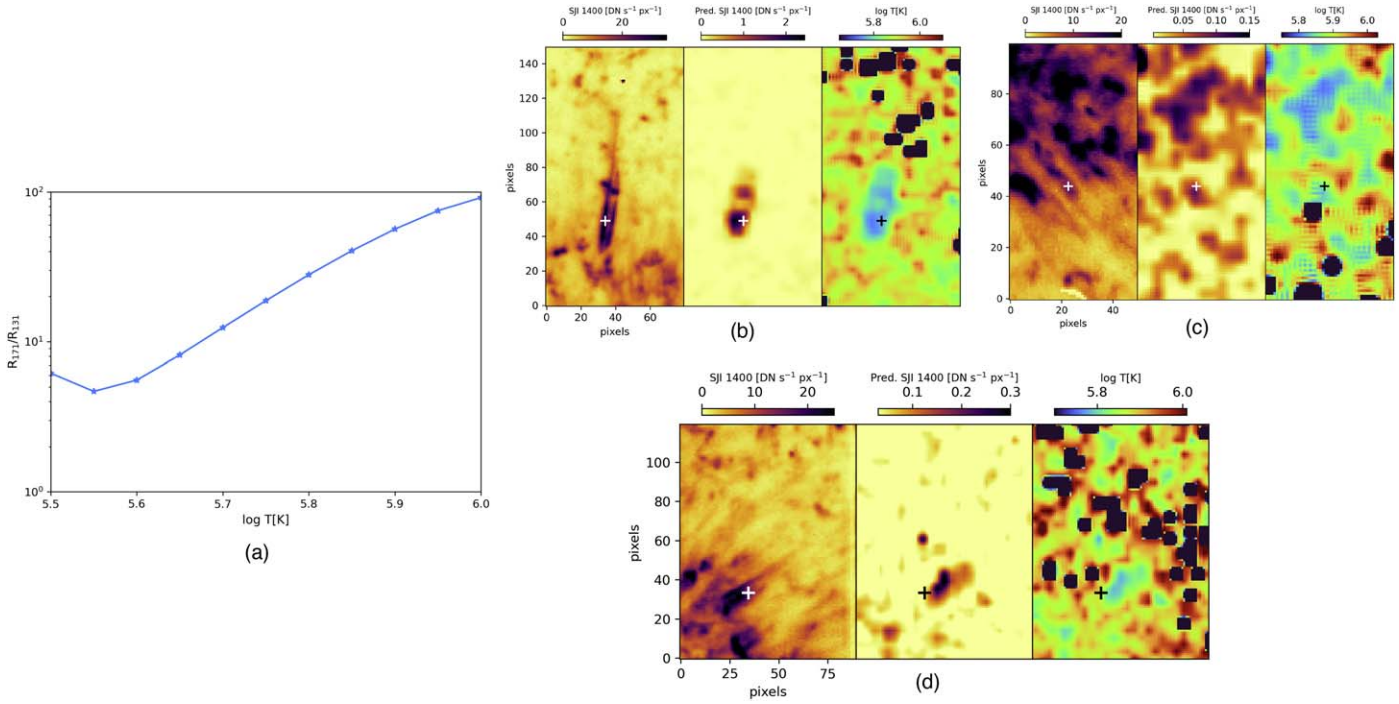

Figure 10. Temperature diagnostics with the filter-ratio method. Panel (a): ratio of the temperature response of the SDO/AIA 171 and 131 filters between log$T$ [K] = [5.5, 6.0]. Panel (b), left to right: observed IRIS Si IV 1400 SJI intensities for network jet 1, predicted intensities using the total EM, and temperature map derived from the filter-ratio technique. Panels (c) and (d) are the same as panel (b) but for network jets 2 and 3. The FOV and the pixel size are the same as Figures 7, 8, and 9.

Appendix B
Supplementary Figures

Upper chromospheric velocities associated with spicules lying at the coronal footpoints derived from the Doppler shift of the Mg II k_3 core as described in the text. The left and the right panels of Figure 11 show the propagation of spicules (visualized by the spacetime maps in the bottom rows and the associated animation) and their LOS velocities in the QS data set corresponding to the same region of interest as Figure 3. Figure 12 shows a zoom-in to enhanced spicular activity and their associated LOS velocities for the area bounded by the solid horizontal lines in Figure 4 for the CH data set.

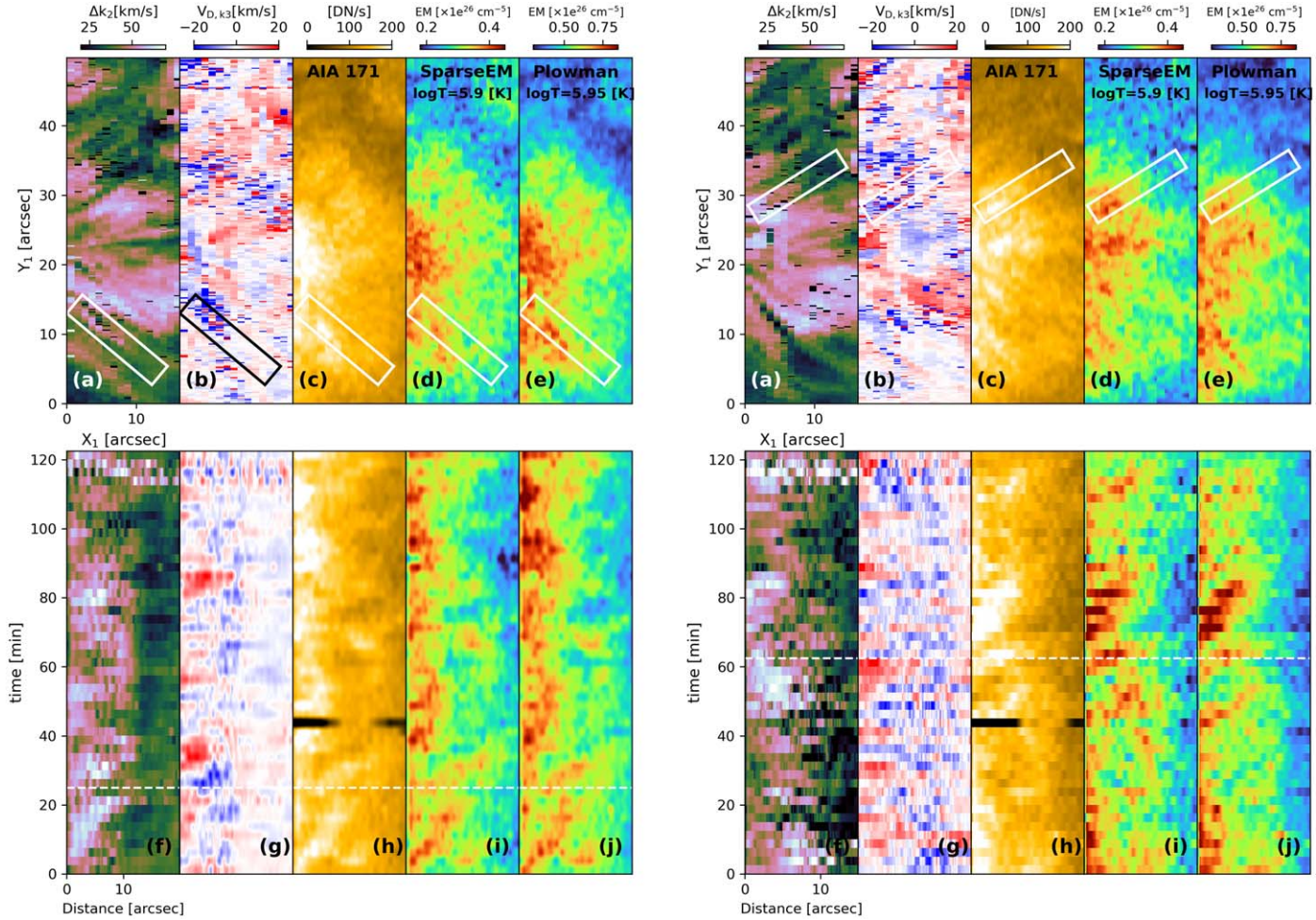

Figure 11. Connecting chromospheric Doppler shifts and emission in the lower corona for the same FOV as in Figure 3. Left column, (a): Mg II k_2 peak separation, (b): Doppler shift of the line core (k_3), (c)–(e): synthetic SDO/AIA 171, and EM rasters corresponding to the IRIS rasters. The rectangular boxes in (a)–(e) show the FOV from which the spacetime maps shown in panels (f)–(j) are derived. Right column: same as the left column except for the bottom row panels (f)–(j), which show the spacetime maps corresponding to the other rectangular box in the top row. An animation showing the temporal evolution of the two columns is available in the online journal.

(An animation of this figure is available in the online article.)

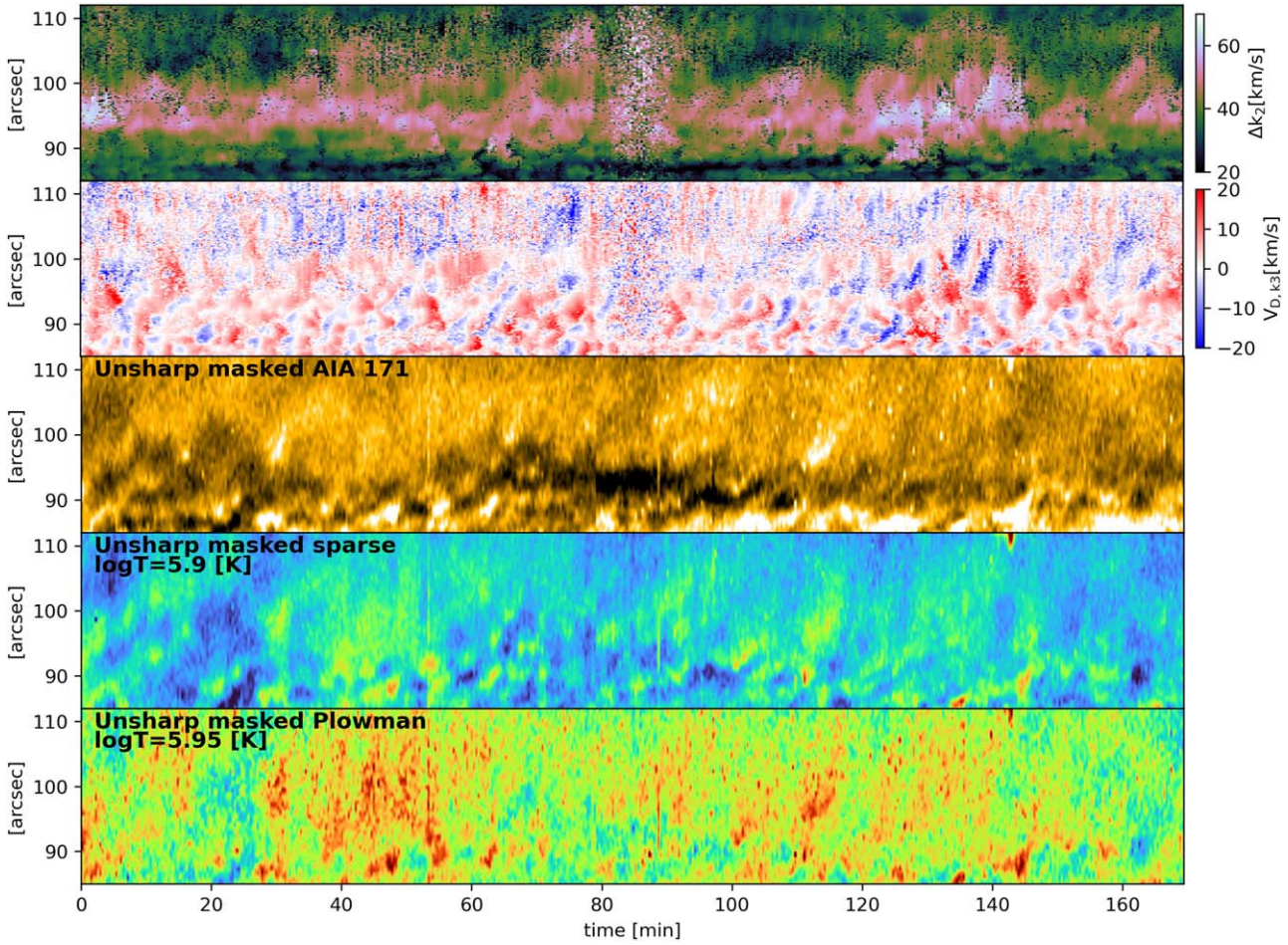

Figure 12. Zoom-in to the chromospheric Doppler shifts and lower coronal emission associated with spicular plasma for the bounded region indicated in Figure 4. Rows from top to bottom show Mg II k_2 peak separation map, Doppler shift of the line core (k_3), unsharped masked version of SDO/AIA 171, EMs computed using the method of sparsity, and Tikhonov regularization.

ORCID iDs

Souvik Bose https://orcid.org/0000-0002-2180-1013
Jayant Joshi https://orcid.org/0000-0003-0585-7030
Paola Testa https://orcid.org/0000-0002-0405-0668
Bart De Pontieu https://orcid.org/0000-0002-8370-952X

References

Asplund, M., Amarsi, A. M., & Grevesse, N. 2021, A&A, 653, A141
Athay, R. G., & Holzer, T. E. 1982, ApJ, 255, 743
Barnes, W. T., Cheung, M. C. M., Bobra, M. G., et al. 2020, JOSS, 5, 2801
Beckers, J. M. 1972, ARA&A, 10, 73
Boerner, P., Edwards, C., Lemen, J., et al. 2012, SoPh, 275, 41
Bose, S., Henriques, V. M. J., Joshi, J., & Rouppe van der Voort, L. 2019, A&A, 631, L5
Bose, S., Joshi, J., Henriques, V. M. J., & Rouppe van der Voort, L. 2021a, A&A, 647, A147
Bose, S., Nóbrega-Siverio, D., De Pontieu, B., & Rouppe van der Voort, L. 2023, ApJ, 944, 171
Bose, S., Rouppe van der Voort, L., Joshi, J., et al. 2021b, A&A, 654, A51
Bryans, P., McIntosh, S. W., De Moortel, I., & De Pontieu, B. 2016, ApJL, 829, L18
Carlsson, M., De Pontieu, B., & Hansteen, V. H. 2019, ARA&A, 57, 189
Cheung, M. C. M., Boerner, P., Schrijver, C. J., et al. 2015, ApJ, 807, 143
Chintzoglou, G., De Pontieu, B., Martínez-Sykora, J., et al. 2021, ApJ, 906, 82
Cho, K.-S., Kumar, P., Cho, I.-H., et al. 2023, ApJ, 953, 69
Cirtain, J. W., Del Zanna, G., DeLuca, E. E., et al. 2007, ApJ, 655, 598
De Pontieu, B., De Moortel, I., Martinez-Sykora, J., & McIntosh, S. W. 2017a, ApJL, 845, L18
De Pontieu, B., Martínez-Sykora, J., & Chintzoglou, G. 2017b, ApJL, 849, L7
De Pontieu, B., Martínez-Sykora, J., Testa, P., et al. 2020, ApJ, 888, 3
De Pontieu, B., McIntosh, S., Hansteen, V. H., et al. 2007, PASJ, 59, S655
De Pontieu, B., & McIntosh, S. W. 2010, ApJ, 722, 1013
De Pontieu, B., McIntosh, S. W., Carlsson, M., et al. 2011, Sci, 331, 55
Del Zanna, G., & Mason, H. E. 2018, LRSP, 15, 5
De Pontieu, B., Testa, P., Martínez-Sykora, J., et al. 2022, ApJ, 926, 52
De Pontieu, B., Title, A. M., Lemen, J. R., et al. 2014, SoPh, 289, 2733
Dere, K. P., Bartoe, J. D. F., & Brueckner, G. E. 1989, SoPh, 123, 41
Dere, K. P., Del Zanna, G., Young, P. R., & Landi, E. 2023, ApJS, 268, 52
Gorman, J., Chitta, L. P., & Peter, H. 2022, A&A, 660, A116
Harris, C. R., Millman, K. J., van der Walt, S. J., et al. 2020, Natur, 585, 357
Henriques, V. M. J., Kuridze, D., Mathioudakis, M., & Keenan, F. P. 2016, ApJ, 820, 124
Herde, V. L., Chamberlin, P. C., Schmit, D., et al. 2023, ApJ, 946, 103
Hinode Review Team, Al-Janabi, K., Antolin, P., et al. 2019, PASJ, 71, R1
Hunter, J. D. 2007, CSE, 9, 90
Judge, P. G., & Carlsson, M. 2010, ApJ, 719, 469
Kayshap, P., Murawski, K., Srivastava, A. K., & Dwivedi, B. N. 2018, A&A, 616, A99
Klimchuk, J. A. 2012, JGRA, 117, A12102
Krishna Prasad, S., Banerjee, D., Van Doorsselaere, T., & Singh, J. 2012, A&A, 546, A50
Lemen, J. R., Title, A. M., Akin, D. J., et al. 2012, SoPh, 275, 17
Madjarska, M. S., Vanninathan, K., & Doyle, J. G. 2011, A&A, 532, L1
Mandal, S., Peter, H., Chitta, L. P., et al. 2023, A&A, 678, L5
Martínez-Sykora, J., De Pontieu, B., De Moortel, I., Hansteen, V. H., & Carlsson, M. 2018, ApJ, 860, 116
Martínez-Sykora, J., De Pontieu, B., Hansteen, V. H., et al. 2017, Sci, 356, 1269
Martínez-Sykora, J., De Pontieu, B., Testa, P., & Hansteen, V. 2011, ApJ, 743, 23
Martínez-Sykora, J., Leenaarts, J., De Pontieu, B., et al. 2020, ApJ, 889, 95
Narang, N., Arbacher, R. T., Tian, H., et al. 2016, SoPh, 291, 1129

Narukage, N., Sakao, T., Kano, R., et al. 2011, SoPh, 269, 169
O'Dwyer, B., Del Zanna, G., Mason, H. E., Weber, M. A., & Tripathi, D. 2010, A&A, 521, A21
Pereira, T. M. D., De Pontieu, B., & Carlsson, M. 2012, ApJ, 759, 18
Pereira, T. M. D., De Pontieu, B., Carlsson, M., et al. 2014, ApJL, 792, L15
Pereira, T. M. D., Leenaarts, J., De Pontieu, B., Carlsson, M., & Uitenbroek, H. 2013, ApJ, 778, 143
Pesnell, W. D., Thompson, B. J., & Chamberlin, P. C. 2012, SoPh, 275, 3
Plowman, J., & Caspi, A. 2020, ApJ, 905, 17
Rouppe van der Voort, L., De Pontieu, B., Pereira, T. M. D., Carlsson, M., & Hansteen, V. 2015, ApJL, 799, L3
Rouppe van der Voort, L., Leenaarts, J., de Pontieu, B., Carlsson, M., & Vissers, G. 2009, ApJ, 705, 272
Samanta, T., Pant, V., & Banerjee, D. 2015, ApJL, 815, L16
Samanta, T., Tian, H., Yurchyshyn, V., et al. 2019, Sci, 366, 890
Schmit, D., Bryans, P., De Pontieu, B., et al. 2015, ApJ, 811, 127
Sekse, D. H., Rouppe van der Voort, L., De Pontieu, B., & Scullion, E. 2013, ApJ, 769, 44
Skogsrud, H., Rouppe van der Voort, L., & De Pontieu, B. 2016, ApJ, 817, 124
Sow Mondal, S., Klimchuk, J. A., & Sarkar, A. 2022, ApJ, 937, 71
Sterling, A. C. 2000, SoPh, 196, 79
Testa, P., & Reale, F. 2020, ApJ, 902, 31
Tian, H., DeLuca, E. E., Cranmer, S. R., et al. 2014, Sci, 346, 1255711
Tripathi, D., & Klimchuk, J. A. 2013, ApJ, 779, 1
Virtanen, P., Gommers, R., Oliphant, T. E., et al. 2020, NatMe, 17, 261
Vissers, G., & Rouppe van der Voort, L. 2012, ApJ, 750, 22
Withbroe, G. L. 1983, ApJ, 267, 825
Young, P. R., Keenan, F. P., Milligan, R. O., & Peter, H. 2018, ApJ, 857, 5